Available online at www.sciencedirect.com
SCIENCE DIRECT
Journal of Membrane Science 268 (2006) 150–164
journal of MEMBRANE SCIENCE
www.elsevier.com/locate/memsci

Phase field simulations of early stage structure formation during immersion precipitation of polymeric membranes in 2D and 3D

Bo Zhou, Adam C. Powell*

Department of Materials Science and Engineering, Massachusetts Institute of Technology, 77 Massachusetts Ave. Rm. 4-117, Cambridge, MA 02139, USA

Received 22 June 2004; received in revised form 15 March 2005; accepted 15 May 2005
Available online 30 August 2005

Abstract

The immersion precipitation process makes most commercial polymeric membranes, which enjoy widespread use in water filtration and purification. In this work, a ternary Cahn–Hilliard formulation incorporating a Flory–Huggins homogeneous free energy function is used to simulate the liquid–liquid demixing stage of the immersion precipitation process, which determines much of the final morphology of membranes. Simulations start with a non-solvent/solvent/polymer ternary system with periodic boundary conditions and uniform initial conditions with small random fluctuations in two-dimensional (2D). Results in 2D demonstrate the effects of M_{ij} (mobilities) and K_{ij} (gradient penalty coefficients) on phase separation behavior. A two-layer polymer–solvent/non-solvent initial condition is then used to simulate actual membrane fabrication conditions. 2D and 3D simulation results show an asymmetric structure of membrane morphology, which strongly agrees with the experimental observation. Then this system is coupled with the Navier–Stokes equations to model hydrodynamics in two dimensions. The results show that fluid flow destabilizes the top layer of membrane.

Keywords: Immersion precipitation; Polymeric membrane; Ternary Cahn–Hilliard; Spinodal decomposition; Fluid flow

1. Introduction

Polymeric membranes have been developed for a variety of industrial applications, including microfiltration, ultrafiltration and reverse osmosis [1]. Each application imposes specific requirements on the membrane material and pore structure. The final morphologies of the membranes will vary greatly, depending on the properties of the materials and the processing conditions. Most commercial membranes are prepared by the immersion precipitation process. In this process, a homogeneous polymer solution is cast on a substrate and then immersed into a coagulation bath containing a non-solvent (usually water). The non-solvent begins to diffuse into the polymer solution and the solvent begins to diffuse into the coagulation bath, while the polymer diffuses very little due to its low mobility. The inter-diffusion of non-solvent and solvent brings the composition of the polymer solution into the miscibility gap of the corresponding ternary phase diagram. Hence, the homogeneous polymer solution starts to decompose into two phases: a polymer-rich phase and a polymer-poor phase. At a certain stage during phase demixing, the polymer-rich phase is solidified into a solid matrix by crystallization or vitrification, while the polymer-poor phase develops into pores. The performance of this membrane depends largely on the morphology formed during phase separation and solidification.

The thermodynamic basis of immersion precipitation, which is the free energy function and the phase diagram of the non-solvent/solvent/polymer ternary system, is well developed [2–4]. Some mass transfer models in 1D have been done to understand the kinetics of the immersion precipitation process before phase separation happens [5–9]. A small number of studies have looked at the onset of phase separation. Saxena and Caneba [10] used a 1D phase field model based on the Cahn–Hilliard equation incorporating the Flory–

* Corresponding author. Tel.: +1 617 452 2086; fax: +1 617 253 5418.
E-mail address: hazelsct@mit.edu.

0376-7388/$ – see front matter © 2005 Elsevier B.V. All rights reserved.
doi:10.1016/j.memsci.2005.05.030

Nomenclature

D_{ij}	diffusivity of species i in the matrix of species j
E	energy
f	homogeneous free energy density
F	total free energy
$\vec{F}$	force per unit volume
Fp	dimensionless force parameter
K_{ij}	gradient penalty coefficient
K_ij	dimensionless gradient penalty coefficient
L	characteristic length scale of simulation domain
m_i	degree of polymerization of component i
M_{ij}	mobility of species i due to a gradient in species j chemical potential
M_ij	dimensionless mobility
R	gas constant (8.314 J/K/mol)
Sc	Schmidt number
t	time
$\overline{t}$	characteristic diffusion time scale of polymer ($L^2/\langle D_{pp}\rangle$)
$\tilde{t}$	dimensionless time
T	temperature
u	velocity in x direction
v	velocity in y direction
v_{site}	volume per reference site
V	total volume

Greek letters

φ_i	volume fraction of component i
λ	dominant wavelength
μ_i	chemical potential of component i
ω	vorticity
Ψ	dimensionless Flory–Huggins free energy density

Subscripts

p	polymer
s	solvent
n	non-solvent

Huggins free energy model to simulate phase separation in the membrane and showed 1D periodicity of concentration profile during the initial stage of decomposition. Barton and McHugh used the Cahn–Hilliard equations in a ternary system, but the concentrations are constrained to change only along a tie line across the miscibility gap, to study membrane formation by thermal quenching, and showed the coarsening rate of the particle size in the late stage follows the 1/3 power law [11–13]. In 2002, Akthakul et al. [14] showed experimental evidence of pore formation via spinodal decomposition in asymmetric membrane formation and then used the Lattice Boltzmann method to simulate membrane formation in 2D [15]. The simulation results captured motion of the interface between coagulation bath and polymer solution and the asymmetric morphology of membranes.

However, the Lattice Boltzmann method is strongly anisotropic, causing the final result to exhibit a morphological bias in the diagonal direction. Furthermore, Lattice Boltzmann requires a regular lattice, which makes it difficult to apply on the irregular simulation domain. Extending to 3D is also not straightforward since there is no regular lattice which could produce isotropic results in 3D. The inherently 3D nature of the process and final product, with connected solid and pore phases, requires a 3D model which can simulate the whole process in the ternary system.

Toward that end, the present work provides a methodology capable of simulating the entire process of membrane structure formation via spinodal decomposition [14]. A single set of partial differential equations simulates the initial diffusion and liquid–liquid phase separation steps using a complete ternary description of the system in two and three dimensions. This will later be extended to solidification of the polymer-rich phase to lock in the membrane structure. In the model, a ternary Cahn–Hilliard phase field formulation incorporating a Flory–Huggins homogeneous free energy function is used to model the phase behavior in this heterogeneous kinetic system. The theory of phase field is discussed in Section 2, including the derivation of the governing equations and the assumptions of the model. Then, the simulation results are presented in Section 3. The first simulations presented begin with uniform initial conditions with small random fluctuations in 2D, later simulations start with two-layer polymer–solvent/non-solvent initial conditions to simulate actual membrane fabrication conditions in 2D and 3D. Then, hydrodynamic effects are added to the 2D system by coupling with fluid flow driven by surface tension. Model limitations and future work are discussed in 4. Finally, the work is concluded in Section 5.

It is worth noting here that the present work is limited to uniform mobilities and viscosities, though with different mobilities for the polymer and solvent. While non-uniform properties are necessary for accurate simulation of the physical system, many important features of the process can be explained by this model even with uniform properties. Furthermore, non-uniform mobility in particular adds considerable complexity to the system behavior, and will be addressed in a separate paper.

2. Theory

2.1. Ternary phase field model

In modeling studies on immersion precipitation, it is common to separate the initial diffusion and phase separation steps into two distinct processes since they appear to be very different phenomena. However, they share the same underly-

ing principles, as they are both driven by minimizing the free energy, which can be described by a phase field model.

Phase field is a very promising methodology for modeling phase transformations involving topological changes and material flux across interfaces. This methodology is built on work involving kinetics of spinodal decomposition beginning with Cahn, Hilliard and Allen from the 1950s through the 1970s [16–18], in which the interface between separating phases is described as "diffuse" with non-zero thickness, instead of sharp. In the past 15 years, phase field has been used to model phenomena from dendritic solidification [19–22], martensitic transformations [23] and grain growth [24] in metals and ceramics to the work of Saxena and Caneba, and of Barton and McHugh, on spinodal decomposition of polymer systems mentioned above [10–13]. In our study, we applied the phase field method to the non-solvent/solvent/polymer ternary system in the immersion precipitation process.

Phase field modeling for conserved variables (e.g., concentration, volume fraction) is based on Cahn–Hilliard equations, which are diffusion equations with a diffuse interface concept from a gradient penalty term in the total free energy. In this phase field model, one set of ternary Cahn–Hilliard equations is employed to simulate the initial diffusions and the induced liquid–liquid phase separation of the immersion precipitation process, which allows us to understand how the phase separation is induced and how the morphology evolves during the phase separation.

The general Cahn–Hilliard equation is written as the following:

$$\frac{\partial \varphi_i}{\partial t} = \nabla \left(\sum_j M_{ij} \nabla \mu_j \right) \tag{1}$$

Here, M_{ij} is the mobility of species i due to the gradient of a generalized chemical potential μ_j that is defined as the variational derivative of the total free energy F with respect to the volume fraction (generally concentration) of species j:

$$\mu_j = \frac{\delta F}{\delta \varphi_j}. \tag{2}$$

In the Cahn–Hilliard model, the contribution of the gradient energy to the total free energy is included. Therefore, the total free energy is not only a function of the concentration but also a function of its gradient. Considering the gradient energy term in a heterogeneous system with an inversion center and neglecting gradient terms beyond second-order, one can write the total free energy (F) as the integral of the homogeneous free energy density (f) plus gradient energy terms over the space (see Eq. (3)).

$$F = \int \left[f + \frac{1}{2} \sum K_{ij} (\nabla \varphi_i \nabla \varphi_j) \right] \mathrm{d}V \tag{3}$$

Here, φ_i is the volume fraction (generally concentration) of species i and K_{ij} are the gradient penalty coefficients. Theoretically, the gradient penalty coefficients (K_{ij}) are defined as the second derivatives of the total free energy with respect to the concentration gradients as follows:

$$K_{ij} = \left. \frac{\partial^2 F}{\partial(\nabla \varphi_i)\partial(\nabla \varphi_j)} \right|_{\nabla \varphi_i = 0, \nabla \varphi_j = 0} \tag{4}$$

However, practically they are very difficult to determine from experiments, and the choices of these coefficients in prior literatures are quite ambiguous [10,11,25]. For all our simulations, the cross gradient penalty coefficients K_{sp}, K_{ps} were neglected and $K_{\mathrm{ss}} = K_{\mathrm{pp}}$ were set with the same constant values estimated from the work of Saxena and Caneba [10] and tuned based our simulation resolution. More details about $K_{\mathrm{ss}} = K_{\mathrm{pp}}$ will be discussed in the later part of the paper.

The well-known Flory–Huggins free energy model is used for this non-solvent (n)/solvent (s) /polymer (p) ternary system, which gives the homogeneous free energy density f as the following:

$$f = \frac{RT}{v_{\mathrm{site}}} \Psi(\phi_{\mathrm{n}}, m_{\mathrm{n}}, \phi_{\mathrm{s}}, m_{\mathrm{s}}, \phi_{\mathrm{p}}, m_{\mathrm{p}}) \tag{5}$$

where m_i is the number of sites occupied by a molecule of species i and φ_i is the volume fraction of species i. Ψ is the dimensionless homogeneous free energy density:

$$\Psi = \varphi_{\mathrm{n}} \ln \varphi_{\mathrm{n}} + \varphi_{\mathrm{s}} \ln \varphi_{\mathrm{s}} + \frac{\varphi_{\mathrm{p}}}{m_{\mathrm{p}}} \ln \varphi_{\mathrm{p}} + \chi_{\mathrm{ns}} \varphi_{\mathrm{n}} \varphi_{\mathrm{s}} + \chi_{\mathrm{sp}} \varphi_{\mathrm{s}} \varphi_{\mathrm{p}} + \chi_{\mathrm{np}} \varphi_{\mathrm{n}} \varphi_{\mathrm{p}} \tag{6}$$

This is simplified by assuming $m_{\mathrm{n}} = m_{\mathrm{s}} = 1$.

Since there are only two independent variables in a ternary system and it's equivalent to choose any two out of the three variables, we choose the polymer (φ_{p}) and the solvent (φ_{s}) in our simulations in order to capture the mobility differences between the macromolecule and the small molecule. Choosing the non-solvent (φ_{n}) with the right parameters will lead to the same results. We assume constant mobility for simplicity. Therefore, with constant K_{ij} and M_{ij}, and neglecting off-diagonal gradient terms ($K_{\mathrm{sp}} = K_{\mathrm{ps}} = 0$), the Cahn–Hilliard equations for this non-solvent/solvent/polymer system can be written for two independent variables, φ_{p} and φ_{s} as the following:

$$\frac{\partial \varphi_{\mathrm{s}}}{\partial t} = M_{\mathrm{ss}} \left[\nabla^2 \left(\frac{\partial f}{\partial \varphi_{\mathrm{s}}} \right) - K_{\mathrm{ss}} \nabla^2 \nabla^2 \varphi_{\mathrm{s}} \right] + M_{\mathrm{sp}} \left[\nabla^2 \left(\frac{\partial f}{\partial \varphi_{\mathrm{p}}} \right) - K_{\mathrm{pp}} \nabla^2 \nabla^2 \varphi_{\mathrm{p}} \right] \tag{7}$$

$$\frac{\partial \varphi_{\mathrm{p}}}{\partial t} = M_{\mathrm{ps}} \left[\nabla^2 \left(\frac{\partial f}{\partial \varphi_{\mathrm{s}}} \right) - K_{\mathrm{ss}} \nabla^2 \nabla^2 \varphi_{\mathrm{s}} \right] + M_{\mathrm{pp}} \left[\nabla^2 \left(\frac{\partial f}{\partial \varphi_{\mathrm{p}}} \right) - K_{\mathrm{pp}} \nabla^2 \nabla^2 \varphi_{\mathrm{p}} \right] \tag{8}$$

The diffusivity can be evaluated by comparing this with Fick's law for diffusive flux $J_i = -\sum_j D_{ij} \nabla C_j$, which gives:

$$D_{ij} = M_{ij} \frac{\partial^2 f}{\partial \varphi_j^2} \tag{9}$$

Diffusivity D_{ij} is generally not constant according to Eq. (9), although M_{ij} is assumed to be constant. During the immersion stage, gradient penalty terms contribute little to the total free energy with a positive D_{ij}, such that Eqs. (7) and (8) technically reduce to the typical diffusion equations. However, during phase separation when the system enters the spinodal region, $\frac{\partial^2 f}{\partial \varphi_j^2}$ becomes negative and the traditional diffusion equation is ill-posed. But the Cahn–Hilliard can describe the "up-hill" diffusion very well because the fourth-order term has the effect of stabilizing the shortest wavelengths. Therefore, one set of Cahn–Hilliard equations can model both initial diffusion and phase separation in the immersion precipitation process.

2.2. Dimensional analysis

Eqs. (7) and (8) are scaled with the following dimensionless variables:

$$\tilde{r} = \frac{r}{L} \tag{10}$$

$$\tilde{t} = \frac{t}{\bar{t}} = \frac{t}{L^2/\langle D_{\mathrm{pp}} \rangle} = \frac{t}{L^2/M_{\mathrm{pp}} \langle f'' \rangle} = \frac{M_{\mathrm{pp}} RT}{v_{\mathrm{site}}} \left\langle \frac{\partial^2 \Psi}{\partial \varphi_{\mathrm{p}}^2} \right\rangle \tag{11}$$

where the length scale L is the width of the domain in 2D simulations (slightly larger in 3D). That width in turn is chosen to be roughly 10–20 times of the initial spinodal decomposition wavelength, in order to efficiently approach the limit of an infinite system while using periodic boundary conditions. $\bar{t}$ is defined as the characteristic diffusion time scale of polymer ($L^2/\langle D_{\mathrm{pp}} \rangle$), as the polymer diffuses most slowly in the system. Choosing the polymer–polymer diffusion constant to scale the time would allow us the capture the controlling kinetics and accelerate the computation considerably by scaling terms to the order of magnitude of one.

According to Eqs. (5) and (9), $\langle D_{\mathrm{pp}} \rangle = M_{\mathrm{pp}} \langle f'' \rangle = \frac{M_{\mathrm{pp}} RT}{v_{\mathrm{site}}} \langle \Psi'' \rangle = \frac{M_{\mathrm{pp}} RT}{v_{\mathrm{site}}} \langle \frac{\partial^2 \Psi}{\partial^2 \varphi_{\mathrm{p}}} \rangle$, where $\langle \Psi'' \rangle$ is the characteristic value of the second derivative of the dimensionless homogeneous free energy density with respect to the volume fraction of the polymer. Dimensionless free energy density Ψ is a function of φ_{s} and φ_{p}; the value of its second derivative is not constant, so choosing a "characteristic value" is not easy. In order to choose a value, we plotted Ψ'' versus φ_{p} in the polymer/non-solvent binary with constant Flory–Huggins parameter of 0.6, and the value of Ψ'' is centered around 0.5. Therefore, we took $\langle \Psi'' \rangle$ as 0.5, and used this value for all of the simulations for simplicity and consistency.

When Eqs. (10) and (11) are substituted into Eqs. (7) and (8), the non-dimensionalized Cahn–Hilliard equations are as follows:

$$\frac{\partial \varphi_{\mathrm{s}}}{\partial \tilde{t}} = M\_\mathrm{ss} \left[\tilde{\nabla}^2 \left(\frac{\partial \Psi}{\partial \varphi_{\mathrm{s}}} \right) - K\_\mathrm{ss}\, \tilde{\nabla}^2 \tilde{\nabla}^2 \varphi_{\mathrm{s}} \right] + M\_\mathrm{sp} \left[\tilde{\nabla}^2 \left(\frac{\partial \Psi}{\partial \varphi_{\mathrm{p}}} \right) - K\_\mathrm{pp}\, \tilde{\nabla}^2 \tilde{\nabla}^2 \varphi_{\mathrm{p}} \right] \tag{12}$$

$$\frac{\partial \varphi_{\mathrm{p}}}{\partial \tilde{t}} = M\_\mathrm{ps} \left[\tilde{\nabla}^2 \left(\frac{\partial \Psi}{\partial \varphi_{\mathrm{s}}} \right) - K\_\mathrm{ss}\, \tilde{\nabla}^2 \tilde{\nabla}^2 \varphi_{\mathrm{s}} \right] + M\_\mathrm{pp} \left[\tilde{\nabla}^2 \left(\frac{\partial \Psi}{\partial \varphi_{\mathrm{p}}} \right) - K\_\mathrm{pp}\, \tilde{\nabla}^2 \tilde{\nabla}^2 \varphi_{\mathrm{p}} \right] \tag{13}$$

with the following denotations:

$$\begin{aligned} \frac{M_{\mathrm{ss}}}{M_{\mathrm{pp}} \langle \Psi'' \rangle} &= M\_\mathrm{ss}, & \frac{K_{\mathrm{ss}}}{L^2 RT/v_{\mathrm{site}}} &= K\_\mathrm{ss} \\ \frac{M_{\mathrm{sp}}}{M_{\mathrm{pp}} \langle \Psi'' \rangle} &= M\_\mathrm{sp}, & \frac{K_{\mathrm{sp}}}{L^2 RT/v_{\mathrm{site}}} &= K\_\mathrm{sp} \\ \frac{M_{\mathrm{ps}}}{M_{\mathrm{pp}} \langle \Psi'' \rangle} &= M\_\mathrm{ps}, & \frac{K_{\mathrm{ps}}}{L^2 RT/v_{\mathrm{site}}} &= K\_\mathrm{ps} \\ \frac{1}{\langle \Psi'' \rangle} &= M\_\mathrm{pp}, & \frac{K_{\mathrm{pp}}}{L^2 RT/v_{\mathrm{site}}} &= K\_\mathrm{pp}. \end{aligned} \tag{14}$$

Two sets of dimensionless parameters M_ij and K_ij need to be determined. $M_$pp is set to be 2 since $\langle \Psi'' \rangle = 0.5$ as discussed before. $M_$sp and $M_$ps are related the flux of one species due to a gradient in the other. For most of the simulations, these are set to zero since the contribution of these cross terms is relatively minor. $M_$ss is chosen to be 1000 times of $M_$pp to capture the relative difference of the mobilities of the polymer and the small molecule. We assume that $K_{\mathrm{ss}} = K_{\mathrm{pp}}$, and estimate their value as 1.6^{-11} based on the work of Saxena and Caneba [10]. After the non-dimensionalization, $K_$ss and $K_$pp are about 10^{-4} to 10^{-5} depending the length scale L, which is chosen to be roughly 10–20 times the initial spinodal decomposition wavelength. Converting the dimensionless results back to the real size is straightforward if the parameters are known.

Another consideration is about the simulation resolution. With the simulation domain size defined as roughly 10 times the initial decomposition wavelength, using 15 grid points per wavelength gives a resolution of 150 grid points across the domain. Thus, the grid dimensions are 150×150 for fully periodic simulations, and 150×300 for membrane simulations which are periodic in x but not y.

2.3. Hydrodynamic effects

Fluid flow is an inherent part of the immersion precipitation process. To capture the hydrodynamic effects, the Navier–Stokes equations are coupled with previous Cahn–Hilliard equations. The equations are coupled by the addition of convective terms to the Cahn–Hilliard equations and include the driving force for reducing free energy at the Cahn–Hilliard diffuse interface in the Navier–Stokes equations.

Following the argument made by Jacqmin [26] for a binary system, the Cahn–Hilliard free energy changes with time due to convection according to:

$$\left.\frac{\partial F}{\partial t}\right|_{\text{convection}} = \int \left[\left.\frac{\delta F}{\delta \varphi_\text{s}}\frac{\partial \varphi_\text{s}}{\partial t}\right|_{\text{convection}} + \left.\frac{\delta F}{\delta \varphi_\text{p}}\frac{\partial \varphi_\text{p}}{\partial t}\right|_{\text{convection}}\right] \mathrm{d}V \quad (15)$$

The variation $\delta F/\delta\varphi_\text{s}$ was defined as μ_s above, and the rate of change of φ_s due to convection is $-\nabla(\vec{u}\varphi_\text{s})$; similar relations hold for φ_p. Thus, integration by parts and the divergence theorem give:

$$\begin{aligned}\left.\frac{\partial F}{\partial t}\right|_{\text{convection}} &= -\int [\mu_\text{s}\nabla(\vec{u}\varphi_\text{s}) + \mu_\text{p}\nabla(\vec{u}\varphi_\text{p})]\,\mathrm{d}V \\ &= -\int_{\text{boundary}} [\mu_\text{s}\vec{u}\varphi_\text{s} + \mu_\text{p}\vec{u}\varphi_\text{p}]\hat{n}\,\mathrm{d}A \\ &\quad + \int [\varphi_\text{s}\vec{u}\nabla\mu_\text{s} + \varphi_\text{p}\vec{u}\nabla\mu_\text{p}]\,\mathrm{d}V \end{aligned} \quad (16)$$

The integral on the boundary vanishes due to the use of periodic and symmetry boundary conditions. This rate of change of Cahn–Hilliard free energy is equal and opposite to the rate of change of kinetic energy due to diffuse surface tension force per unit volume $\vec{F}$, which is:

$$\left.\frac{\partial E}{\partial t}\right|_{\text{kinetic}} = \int \vec{u}\vec{F}\,\mathrm{d}V \quad (17)$$

Therefore, the surface tension forcing term must be given by:

$$\vec{F} = -\sum_i \varphi_i \nabla\mu_i \quad (18)$$

As Jacqmin noted, when used in the velocity-pressure form of the incompressible Navier–Stokes equations, an additional potential must be added to the pressure in order to satisfy the incompressibility constraint.

The resulting system consists of equations of continuity, motion and transport, which for an incompressible fluid in the velocity–vorticity form are as follows:

$$\nabla^2 u + \frac{\partial\omega}{\partial y} = 0 \quad (19)$$

$$\nabla^2 v - \frac{\partial\omega}{\partial x} = 0 \quad (20)$$

$$\frac{\mathrm{D}\omega}{\mathrm{D}t} = \nu\nabla^2\omega + \frac{\nabla\times\vec{F}}{\rho} \quad (21)$$

$$\frac{\mathrm{D}\varphi_i}{\mathrm{D}t} = \nabla\left(\sum_i M_{ij}\nabla\mu_j\right) \quad (22)$$

Here, $\vec{u}$ is the velocity vector, u and v the x and y components of $\vec{u}$, ρ the density, $\vec{F}$ the driving force of the fluid flow, i.e. interface curvature and $\frac{\mathrm{D}}{\mathrm{D}t}$ is the substantial derivative giving by $\frac{\partial}{\partial t} + \vec{u}\nabla$. ω is the vorticity, which is defined as:

$$\omega = \nabla\times\vec{u} = \frac{\partial v}{\partial x} - \frac{\partial u}{\partial y} \quad (23)$$

When Eqs. (19)–(22) are normalized by $\tilde{r} = \frac{r}{L}$, $\tilde{t} = \frac{L^2}{M_\text{pp}\langle f''\rangle}$, $\tilde{u} = \frac{u}{L/t} = \frac{u}{M_\text{pp}\langle f''\rangle/L}$ and $\tilde{\omega} = \frac{\omega}{\omega} = \frac{\omega}{1/t}$, the resulting dimensionless equations are:

$$\tilde{\nabla}^2\tilde{u} + \frac{\partial\tilde{\omega}}{\partial\tilde{y}} = 0 \quad (24)$$

$$\tilde{\nabla}^2\tilde{v} - \frac{\partial\tilde{\omega}}{\partial\tilde{x}} = 0 \quad (25)$$

$$\frac{\partial\omega}{\partial t} + \tilde{\vec{u}}\tilde{\nabla}\tilde{\omega} = Sc\tilde{\nabla}^2\tilde{\omega} + \mathrm{Fp}\tilde{\nabla}\times(\tilde{\vec{F}}) \quad (26)$$

Here, $\tilde{\vec{F}}$ is the dimensionless driving force of the fluid flow. Sc is the Schmidt Number and Fp is a dimensionless force parameter:

$$\begin{aligned}\tilde{\vec{F}} &= -[\varphi_\text{s}\tilde{\nabla}\tilde{\mu}_\text{s} + \varphi_\text{p}\tilde{\nabla}\tilde{\mu}_\text{p}] \\ Sc &= \frac{\eta\bar{t}}{\rho L^2} = \frac{\eta}{\rho\langle D_\text{pp}\rangle} \\ \mathrm{Fp} &= \frac{RTL^2}{\rho\, v_\text{site}\langle D_\text{pp}\rangle^2}\end{aligned} \quad (27)$$

Dimensionless Cahn–Hilliard equations are as before (Eqs. (12) and (13)), but with the substantial derivative indicating convective transport (Eq. (22)).

Although the viscosity is a strong function of polymer volume fraction, the present work assumes it to be constant in all of these simulations. The viscosity change is important to the immersion precipitation process, especially in the case involving the glass transition, and will be addressed in the future.

2.4. Numerical implementation

The Cahn–Hilliard equations (see Eqs. (12) and (13)) were discretized by the Finite Difference method on a regular grid. First order up-winding was used for all convective terms. Crank–Nicholson timestepping was used to discretize time. As described above, the velocity–vorticity form of Navier–Stokes equations was used in order to avoid spurious modes in the traditional velocity–pressure formulation.

For further development, the partial differential equation formulation adopted here permits the use of other efficient computational methods such as finite elements, enabling solution of the equations in irregular geometric domains.

The Portable, Extensible Toolkit for Scientific Computation (PETSc) [27] was used for solving the non-linear system of difference equations in parallel and for distributed storage of the data.

3. Results

3.1. Non-solvent/solvent/polymer ternary system

The model was first tested with a typical non-solvent/solvent/polymer ternary system with $\chi_{ns} = 0.2$, $\chi_{np} = 1$, $\chi_{sp} = 0.3$ and $m_p = 64$. There is a free energy barrier between the non-solvent and the polymer in such a ternary system, which causes the phase separation. Periodic boundary conditions (BC) and the initial condition (IC) of $\varphi_s = \varphi_p = 0.2 \pm 0.005$ (uniform random distribution over this interval) were applied. Other parameters were $M\_pp = 2$, $M\_ss = 2$, $M\_sp = M\_ps = 0$ and $K\_ss = K\_pp = 1.6 \times 10^{-5}$. The grid size is 150×150. The change of the volume fraction of the polymer (φ_p) with time is shown in Fig. 1, where blue stands for $\varphi_p = 1$ and red stands for $\varphi_p = 0$.

According to the given initial condition, the ternary system actually begins within the miscibility gap. The simulation results show the typical spinodal morphology with two separated phases: a polymer-rich phase with high φ_p and a polymer-poor phase with low φ_p (see Fig. 1), which is consistent with the theoretical prediction based on the thermodynamics of the ternary system.

Furthermore, other simulations were run with different mobilities M_{ij} and gradient penalty coefficients K_{ij}. Simulation results with changing M_{ij} indicate that increasing M_ss speeds up phase separation, while increasing M_sp and M_ps slows it down. The volume fraction of the polymer and the solvent both start with 0.2, but they change in the opposite fashion. Therefore, the driving forces (i.e. chemical potentials as defined in the paper) of the solvent and the polymer have the opposite sign. M_{ps} and M_{sp} terms offset the contribution of M_{pp} and M_{ss} terms, and drive the down-hill diffusion during the phase decomposition. So increasing M_{ps} an M_{sp} slows down the kinetics.

Different resulting morphologies (φ_p) of the simulation with different K_ij are shown in Fig. 2. The Fourier transform of the results at the onset of phase separation shows that the dominant dimensionless wavelengths are $\lambda_1 = 0.071429$ and $\lambda_2 = 0.2$ at $K\_pp = 1.6 \times 10^{-5}$ and 1.6×10^{-4}, respectively, while the 1.6×10^{-6} case shows several small peaks around 0.025 indicating insufficient res-

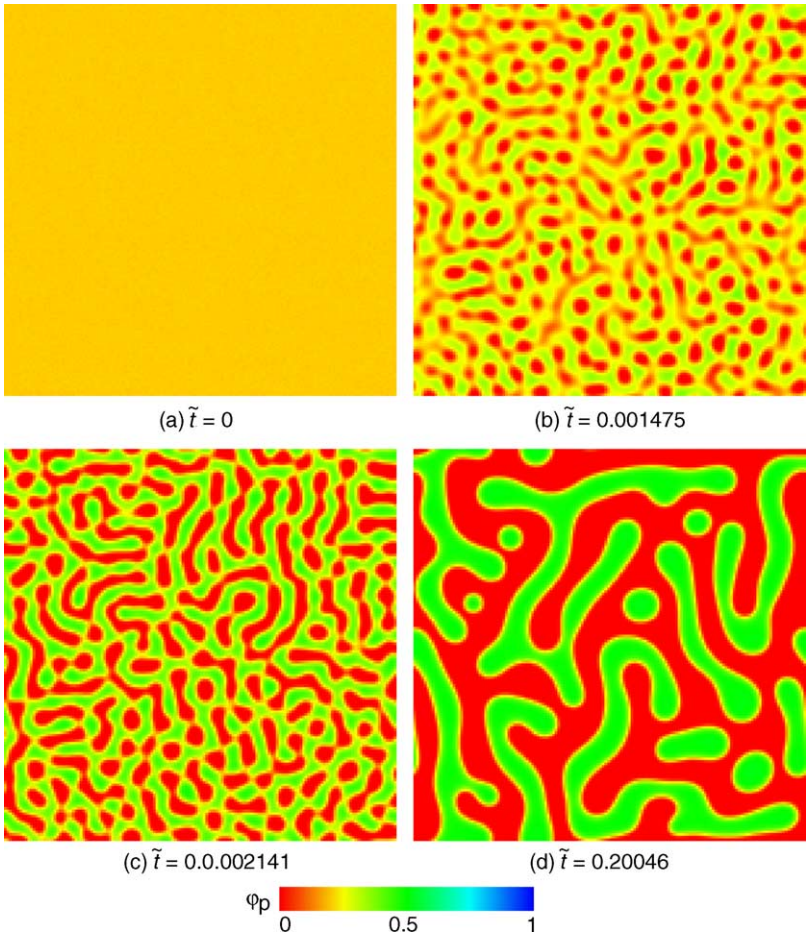

Fig. 1. Spinodal decomposition in the non-solvent/solvent/polymer system with $\chi_{ns} = 0.2, \chi_{np} = 1, \chi_{sp} = 0.3$ and $m_p = 64$.

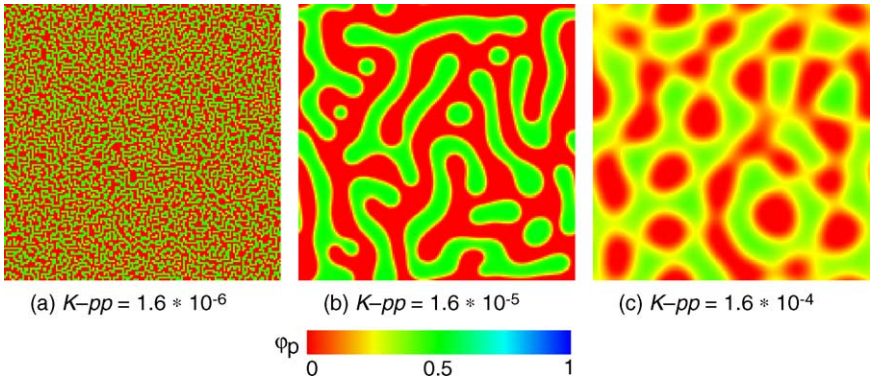

Fig. 2. Membrane morphologies (the volume fraction of the polymer, φ_p) at $\tilde{t} = 0.02$ with different K_ij in the ternary system with $\chi_{ns} = 0.2$, $\chi_{np} = 1$, $\chi_{sp} = 0.3$ and $m_p = 64$, where blue stands for $\varphi_p = 1$ and red stands for $\varphi_p = 0$. (For interpretation of the references to color in this figure legend, the reader is referred to the web version of this article.)

olution. Eyre describes a procedure for estimating interfacial energy and wavelength in a ternary system [28]; roughly speaking, this can be expressed as:

$$\lambda \propto \epsilon \propto \sqrt{\sum_{i,j} K_{ij}} \tag{28}$$

From the simulations, the dimensionless wavelengths are determined by Fourier transform to be $\lambda_1^2 : \lambda_2^2 = 1 : 7.84$, with the dimensionless wavelength at $K\_pp = 1.6 \times 10^{-6}$ showing a similar ratio to λ_1, both of which are not far from to the 1:10 predicted by theory.

3.2. Water/DMF/PVDF membrane system

3.2.1. 2D results

The model was next used to study the water/DMF/PVDF membrane system. Here, water is the non-solvent, dimethylformamide (DMF) the solvent and poly(vinylidene fluoride) (PVDF) the polymer. PVDF membranes can be used for ultrafiltration and microfiltration. The membrane exhibits an asymmetric structure containing a non-porous dense skin and a porous bulk [11]. Concentration-dependent Flory–Huggins interaction parameters of the water (1)/DMF (2)/PVDF (3) ternary system are $\chi_{12} = \frac{-0.058}{1-0.622\times\varphi_2(1-\varphi_3)}$, $\chi_{13} = 3.5$ and $\chi_{23} = -1 + 0.5 \times \varphi_3$ [8].

Fig. 3(a) shows the phase diagram of water/DMF/PVDF system with $m_p = 5$: the calculated spinodal according to Yilmaz and McHugh's method [4] and the binodal drawn based on the equilibrium concentration of the simulation results. Fig. 3(b) shows the calculated spinodal curves for different m_p in the PVDF system. As can be seen from Fig. 3(b), the spinodal curve of $m_p = 10$ is already very close to the solvent axis, indicating that the equilibrium concentration is very small for $m_p = 10$. As m_p goes up, the equilibrium concentration becomes even smaller, increasing computational cost. With this in mind, m_p is chosen to be 5, which is too small for a real polymer molecule, but large enough to capture the phase separation behavior. Other parameters used in simulations were $M\_ss = 2000$, $M\_pp = 2$, $M\_sp = M\_ps = 0$ and $K\_ss = K\_pp = 10^{-4}$. Periodic boundary conditions were applied in the x direction, with zero-flux boundary conditions in the y direction. The initial composition in the polymer solution layer is $\varphi_p = 0.2 \pm 0.005$ and $\varphi_s = 0.75 \pm 0.005$, and in the coagulation bath is $\varphi_p = 0.01 \pm 0.005$ and $\varphi_s = 0.01 \pm 0.005$. The ratio of x dimension to y dimension is 1:2, and the grid size is 150×300.

The morphology evolution (the change of the volume fraction of the polymer (φ_p) with time) is shown in in Fig. 4, where blue stands for $\varphi_p = 1$ and red stands for $\varphi_p = 0$. The

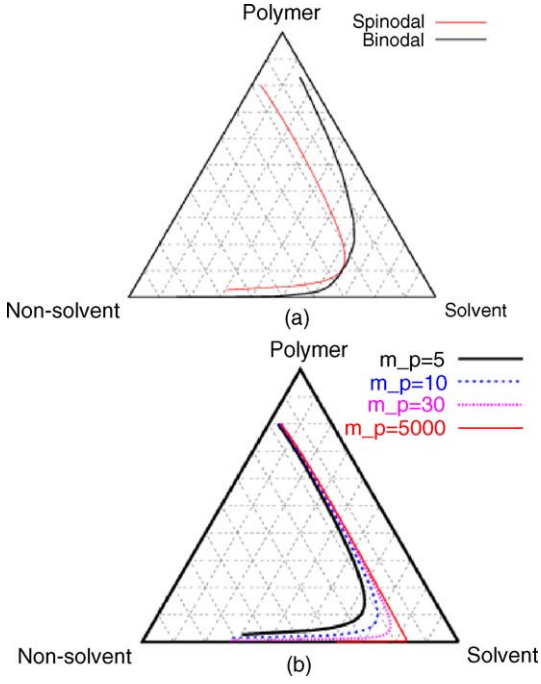

Fig. 3. Phase diagrams of the water/DMF/PVDF system. (a) The phase diagram of Water/DMF/PVDF system with $m_p = 5$: the calculated spinodal according to Yilmaz and McHugh's method [4] and the binodal drawn based on the equilibrium concentration of the simulation results. (b) Calculated spinodal curves for different m_p in the PVDF system according to Yilmaz and McHugh [4].

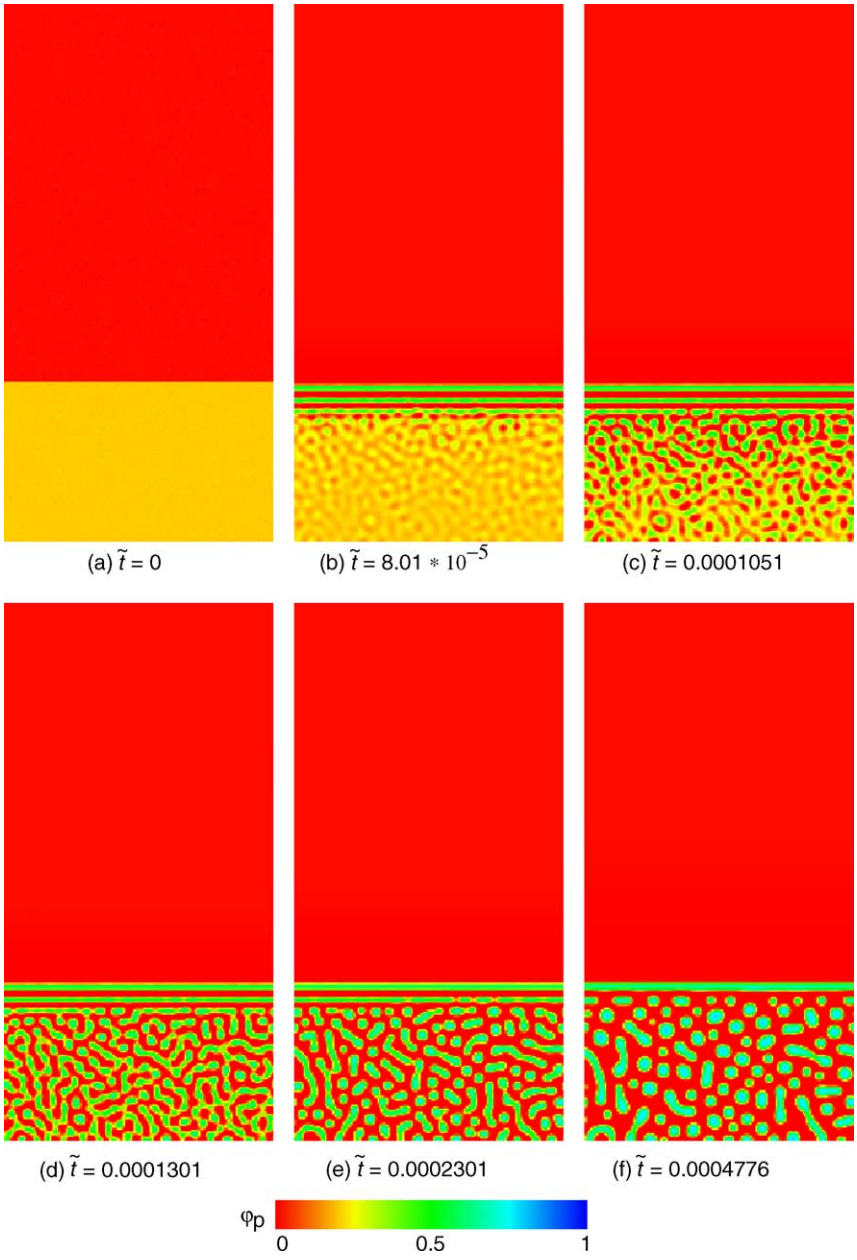

Fig. 4. Morphology evolution (the change of the volume fraction of the polymer, φ_p) during spinodal decomposition of the PVDF membrane system in 2D, where blue stands for $\varphi_p = 1$ and red stands for $\varphi_p = 0$. (For interpretation of the references to color in this figure legend, the reader is referred to the web version of this article.)

system begins with a two-layer initial condition, with polymer solution (polymer and solvent) in the bottom 30% and the coagulation bath (non-solvent) on the top. The solvent and the non-solvent inter-diffuse quickly, but the polymer almost completely stays in the polymer solution area. The polymer is not prohibited from entering the coagulation bath in our model as in Cohen's mass transfer model [5], but it stays in the bottom layer due to the free energy barrier and its low mobility. After some time of inter-diffusion, the composition of the polymer solution enters the spinodal curve shown in Fig. 3(a). Hence, phase separation begins at the top of the polymer solution layer, and proceeds downward in a layered structure. This layered structure is a result of the interaction between the homogeneous and gradient energies driven by the planar interface between the polymer solution and coagulation bath, and is similar to the "short-wavelength composition waves" described by Allen and Cahn in an iron–aluminum system [29]. With time, spinodal decomposition takes place throughout the entire layer, then particles coarsen to continuously reduce the total free energy. The final morphology of the PVDF membrane exhibits an asymmetric structure with a dense skin layer on top of a porous support layer, in strong agreement with experimental observations.

3.2.2. Effects of initial composition

Next, the initial composition was varied either in the polymer solution or in the coagulation bath to study the effect on membrane morphology.

First, two series of simulations were performed with different initial compositions in the polymer solution; those initial compositions are listed in Table 1, while the initial composition in the coagulation bath for all simulations here was $\varphi_{p,\text{bath}} = 0.01$, $\varphi_{s,\text{bath}} = 0.01$ and $\varphi_{n,\text{bath}} = 0.98$. The first series (Cases 1–4) varied φ_p and φ_s in the polymer solution, while keeping φ_n constant. The second series (Cases 1, 5–7) varied φ_s and φ_n in the polymer solution, while keeping φ_p constant.

The simulated morphologies (φ_p) starting with different initial conditions (indicated by points in the phase diagram) are shown in Fig. 5 with the normalized color map, where blue stands for the maximum of φ_p and red stands for the minimum of of φ_p for a better contrast. The blue points present the different *initial conditions* of the simulations in the first series. As can seen from Fig. 5, when increasing the volume frac-

Table 1
Changing initial compositions in the polymer solution

Case	$\varphi_{p,\text{solution}}$	$\varphi_{s,\text{solution}}$	$\varphi_{n,\text{solution}}$
1	0.20	0.75	0.05
2	0.30	0.65	0.05
3	0.35	0.60	0.05
4	0.40	0.55	0.05
5	0.20	0.60	0.20
6	0.20	0.50	0.30
7	0.20	0.35	0.45

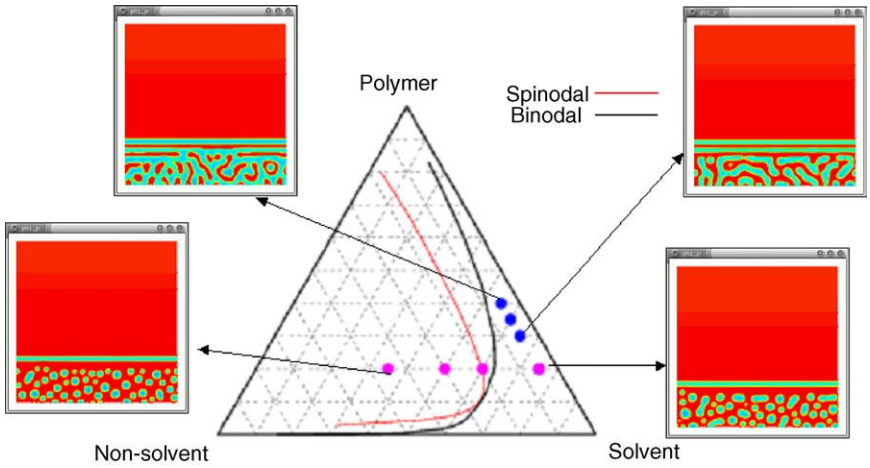

Fig. 5. Effects of changing initial compositions in the polymer solution on PVDF membrane morphology. The membrane morphology is presented by the normalized φ_p with blue as the maximum and red as the minimum. The points in the ternary diagram indicate the initial conditions of the corresponding simulation results. (For interpretation of the references to color in this figure legend, the reader is referred to the web version of this article.)

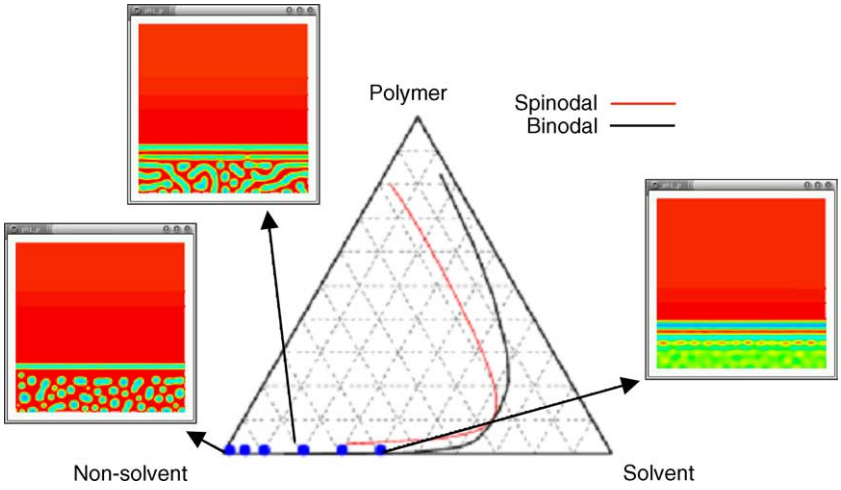

Fig. 6. Effects of changing initial compositions in the coagulation bath on PVDF membrane morphology. The membrane morphology is presented by the normalized φ_p with blue as the maximum and red as the minimum. The points in the ternary diagram indicate the initial conditions of the corresponding simulation results. (For interpretation of the references to color in this figure legend, the reader is referred to the web version of this article.)

tion of the polymer, the resulting morphology changes from isolated droplets to bi-continuous pattern. The second series is indicated by the magenta points that lie in the horizontal direction for the *initial conditions* of each simulation in Fig. 5. Morphology actually does not change significantly when the volume fraction of the solvent decreases, although the final equilibrium concentrations are different. This leads to the conclusion that the volume fraction of the polymer dominates the morphology of membrane since it determines where the system enters the spinodal and the proportion of the two phases.

Second, initial compositions in the coagulation bath were varied as indicated in Table 2, while the initial composition in the polymer solution for all simulations was $\varphi_{p,\text{solution}} = 0.20$, $\varphi_{s,\text{solution}} = 0.75$ and $\varphi_{n,\text{solution}} = 0.05$.

Table 2
Changing initial compositions in the coagulation bath

Case	$\varphi_{p,\text{bath}}$	$\varphi_{s,\text{bath}}$	$\varphi_{n,\text{bath}}$
1	0.01	0.01	0.98
2	0.01	0.05	0.94
3	0.01	0.10	0.89
4	0.01	0.20	0.79
5	0.01	0.30	0.69
6	0.01	0.40	0.59

The simulated morphologies (φ_p) are shown in Fig. 6 with the normalized color representation. The points in the figure represent the *initial conditions* of the simulations. The

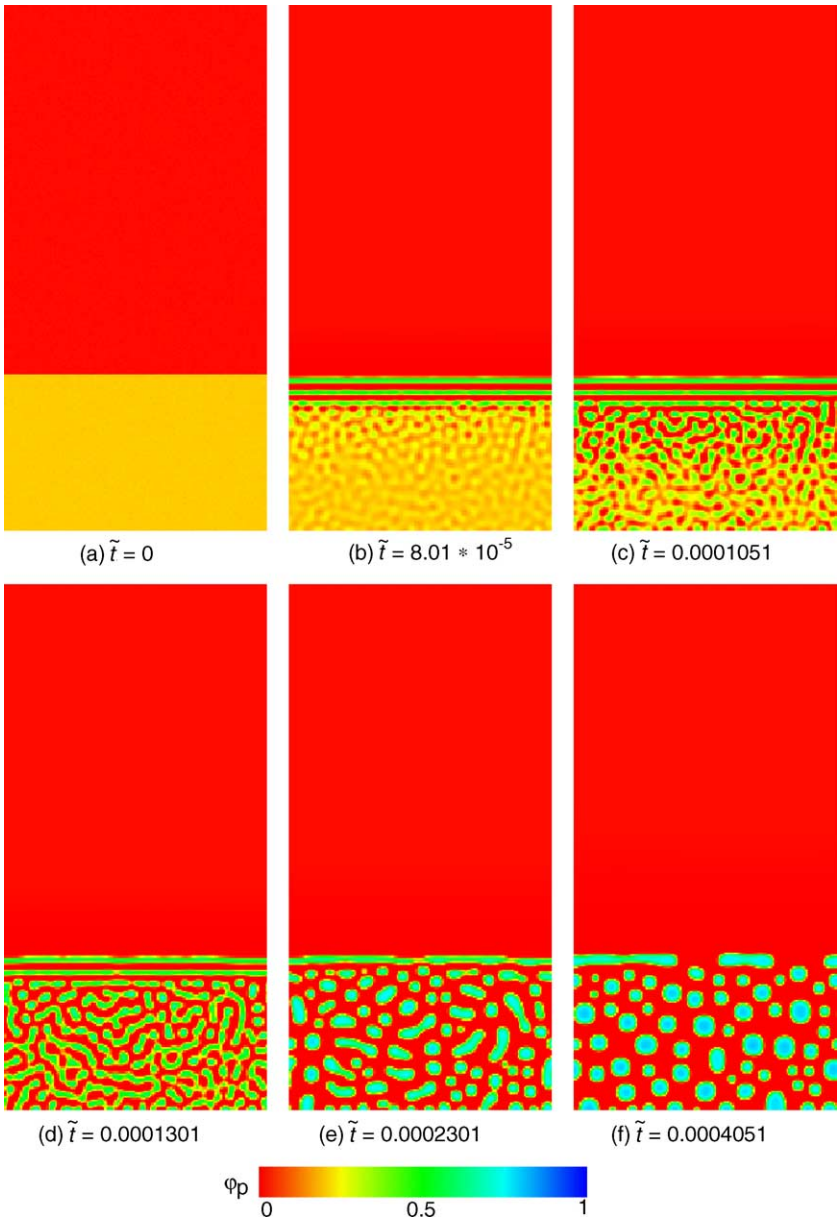

Fig. 7. Morphology evolution (φ_p) of PVDF membrane with fluid flow in 2D, where blue stands for $\varphi_p = 1$ and red stands for $\varphi_p = 0$. (For interpretation of the references to color in this figure legend, the reader is referred to the web version of this article.)

morphology changes from isolated droplets to bi-continuous pattern when increasing the solvent volume fraction in the coagulation bath since it changes the composition in the spinodal where phase separation begins. This also reduces the gradient of the solvent, which delays the onset of phase separation.

3.3. Water/acetone/CA membrane system

The water (1)/acetone (2)/cellulose acetate (CA) (3) ternary system was simulated with the same Cahn–Hilliard parameters except m_p. The Flory–Huggins parameters of the water/acetone/CA system are $\chi_{12} = 0.661 + \frac{0.417}{1-0.755\varphi_2}$, $\chi_{13} = 1.4$ and $\chi_{23} = 0.535 + 0.11\varphi_3$ [7]. Because χ_{13} of water/CA is much smaller than χ_{13} of water/PVDF, CA and water are still miscible when $m_p = 5$, and in fact m_p can be as large as 50 with reasonable computational efficiency. Comparing with the PVDF membrane, the calculated pore size in the CA membrane is about twice that of the PVDF, and phase separation of the CA system is much slower than in the PVDF system; both of these can be understood in terms of the smaller χ_{13} value for this system.

3.4. Hydrodynamic effects

Simulation results with interface-driven fluid flow are as follows. In the first simulation, the Schmidt number (Sc) is set to be 10^3 and the dimensionless force parameter (Fp) to be 10^9, with other parameters as before. The simulation results shown in Fig. 7 indicate that the final morphology is similar to the case without fluid flow, except that the top layer breaks up at some stage of coarsening. This indicates that fluid flow destabilizes the top layer.

Other simulations were run with various values of Sc and Fp. The results are shown in Fig. 8.

Fig. 8 indicates that the top layer is unstable with smaller Sc and larger Fp. When the Schmidt number is larger, the viscosity is larger, therefore, the flow is slower and the top layer is more stable. Increasing the dimensionless force parameter (Fp) implies increasing the surface tension, which drives the flow. This leads to more vigorous flow, which breaks up the top layer.

Furthermore, the data available suggest that the ratio of the Schmidt number to the force parameter determines the stability of the top layer: when that ratio is at or above above 10^{-5}, it is stable; when at or below 10^{-6}, it is unstable. This ratio is related to the capillary number given by:

$$\mathrm{Ca} = \frac{\eta U}{\sigma} \tag{29}$$

where σ is the surface tension and U the characteristic velocity, though there is no distinct characteristic velocity in this system.

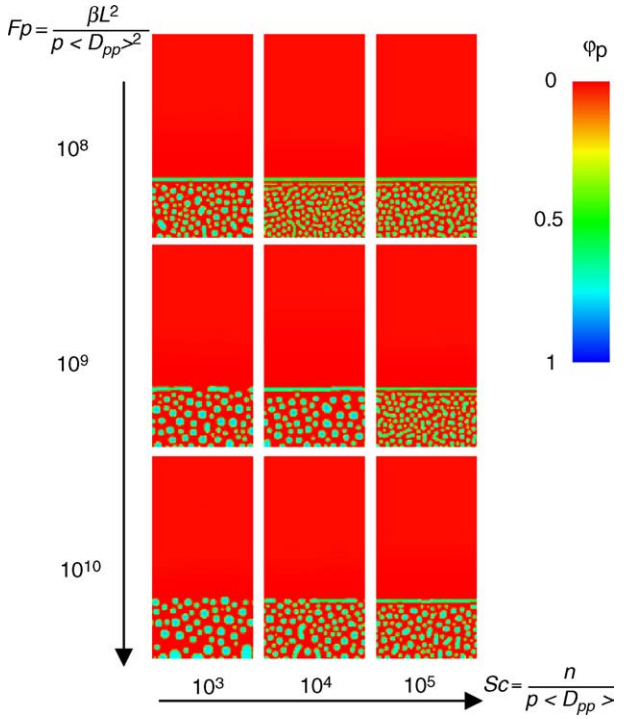

Fig. 8. Morphologies (φ_p) of PVDF membrane with different values of Sc and Fp. The x axis is Sc and the y axis is the dimensionless force parameter, Fp. Blue stands for $\varphi_p = 1$ and red stands for $\varphi_p = 0$. (For interpretation of the references to color in this figure legend, the reader is referred to the web version of this article.)

3.5. 3D PVDF membrane

3.5.1. 3D morphology evolution

A 3D simulation was run with the same m_p, M_ij, K_ij and layer thickness as was used in the 2D PVDF simulation. The dimensionless domain size is $0.45 \times 1 \times 0.45$, and the grid size is $90 \times 200 \times 90$. The formation of the PVDF membrane (the time evolution of φ_p) in 3D is shown in Fig. 9, which shows four contours of the volume fraction of the polymer (φ_p) at 0.2 (red), 0.4 (yellow), 0.6 (green) and 0.8 (cyan) that is approximately the equilibrium concentration of the polymer-rich phase. Like the 2D results, the system begins with a homogeneous polymer solution, then phase separation takes place form the top with a layered structure and continues through out the entire polymer solution area, and finally coarsening increases the domain sizes. The final simulated morphology also shows an asymmetric structure with a dense layer on top of a porous bulk, but with a qualitative difference compared with 2D results: in 3D both polymer-rich and polymer-lean phases are continuous, which is not possible in two dimensions.

3.5.2. Coarsening pattern

In order to understand the pattern of opening and coalescing of pores during membrane formation, the enlarged figures of the morphologies in the polymer solution during

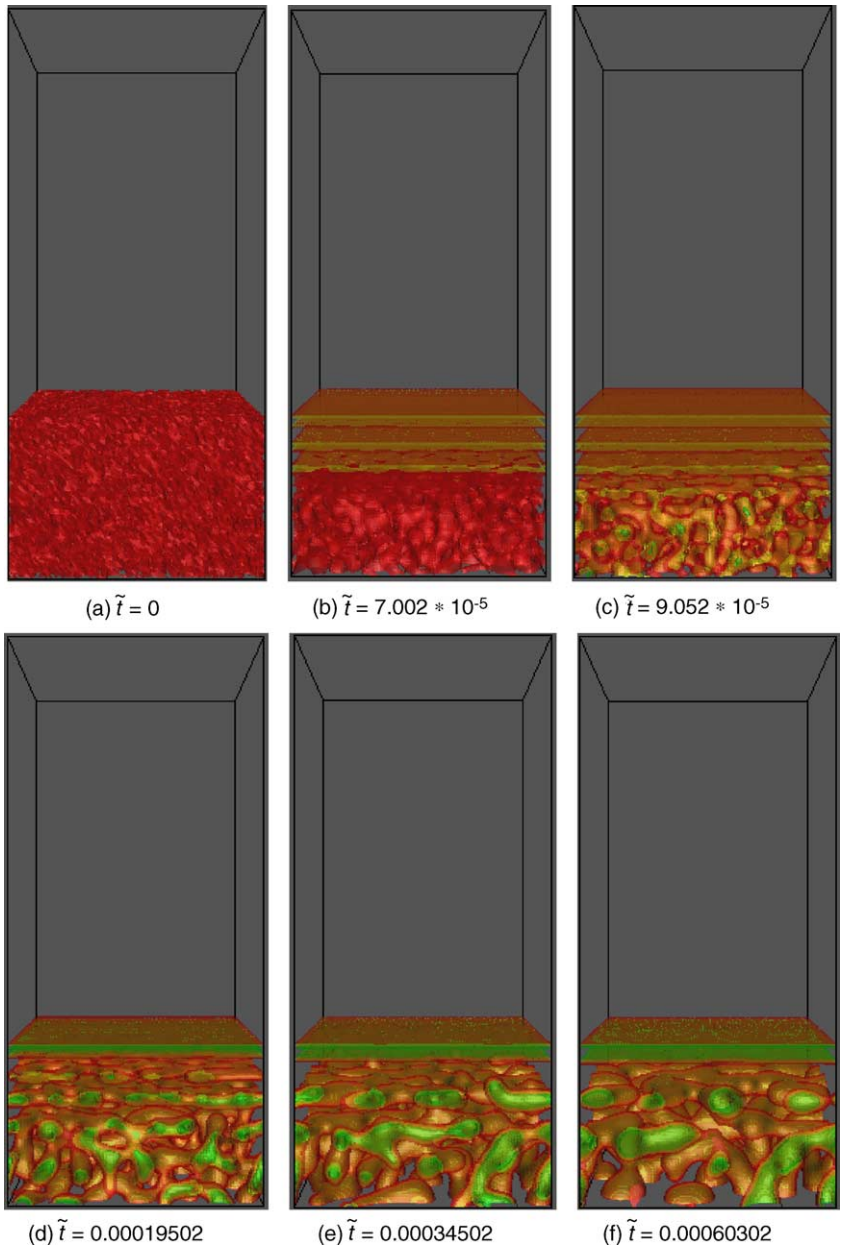

Fig. 9. 3D morphology evolution (φ_p) of PVDF membrane: contours of φ_p at 0.2 (red), 0.4 (yellow), 0.6 (green), 0.8 (cyan). (For interpretation of the references to color in this figure legend, the reader is referred to the web version of this article.)

the coarsening stage are shown in Fig. 10. Attachments from the bottom to the third layer open holes in that layer, then this process repeats with the second layer, which then merges together with the third layer as they coarsen.

3.5.3. Qualitative comparison with experimental results

Fig. 11 shows the comparison between the simulation results with the experimental results given by Cheng et al. [8]. As it can be seen from Fig. 11, the simulation results show an asymmetric membrane structure: a non-porous selective layer (or micro-porous layer which contains pores with much smaller size compared to supporting layer) at the top and the macro-porous supporting layer at the bottom. Furthermore, the simulated morphology of the bottom surface shows qualitative similarity in pore morphology and pore distribution compared with the SEM micrograph Fig. 11(c).

4. Discussion

The model presented here captures a lot of the physical phenomena involved in this process, and can explain some of the physical features present during membrane formation. However, its assumptions impose limits on its predictive capability and accuracy.

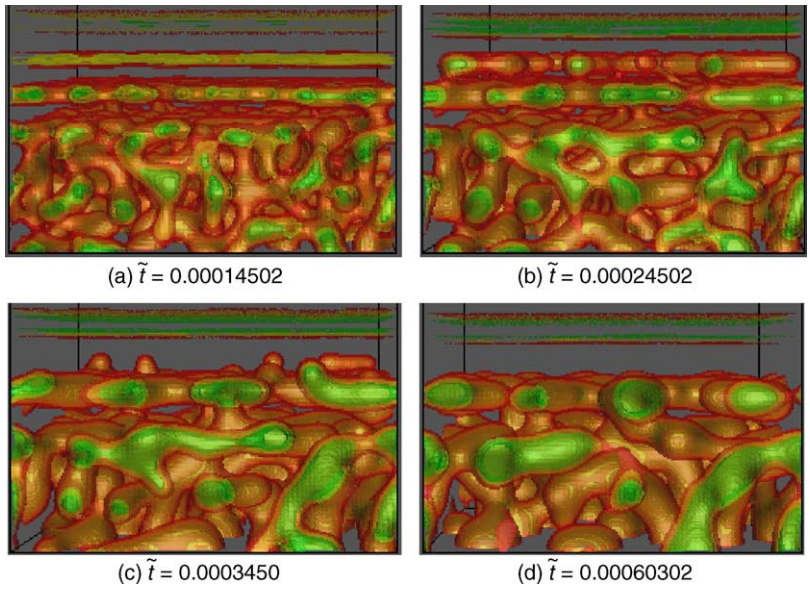

Fig. 10. Coarsening pattern in PVDF membrane: contours of φ_p at 0.2 (red), 0.4 (yellow), 0.6 (green), 0.8 (cyan). (For interpretation of the references to color in this figure legend, the reader is referred to the web version of this article.)

First, the model assumes uniform mobilities and viscosities, though with different mobilities for the polymer and solvent, while both mobilities and viscosities in real systems have a strong dependence on the concentrations. Non-uniform mobility and viscosity in particular adds considerable complexity to the system behavior, and will be addressed in a separate paper. When adopting variable mobilities, we expect to see slower solvent/non-solvent exchange after for-

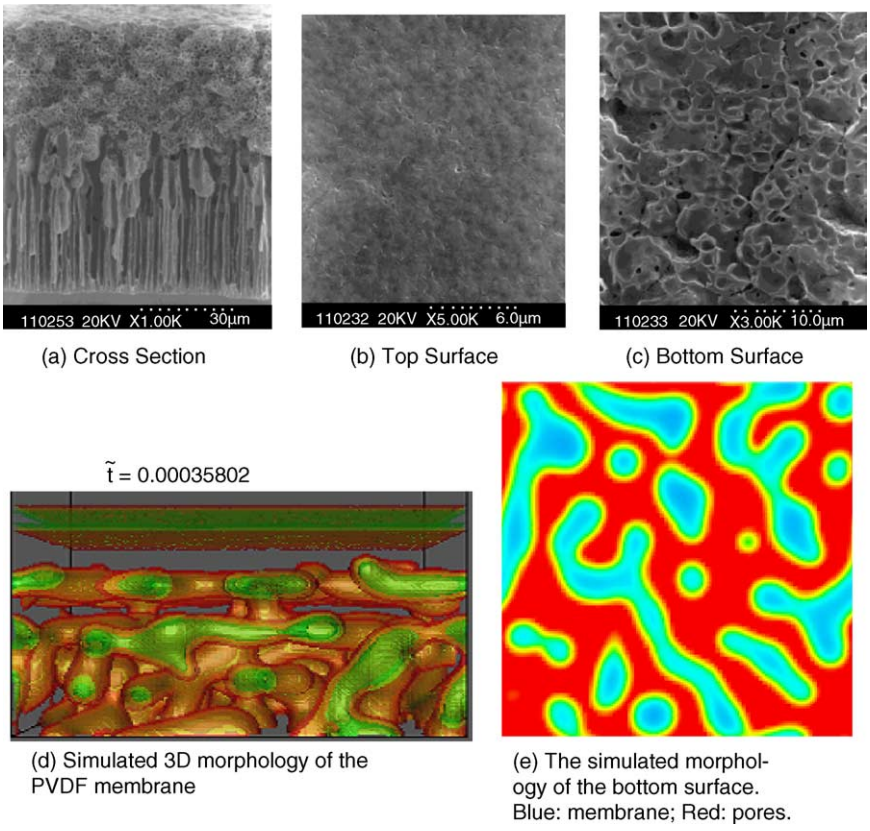

Fig. 11. Comparison of the simulation results with experimental results: (a)–(c)are the SEM Photomicrographs of PVDF membrane prepared by immersion precipitation from the paper of Cheng et al. [8]. (d and e) The simulation results. (For interpretation of the references to color in this figure legend, the reader is referred to the web version of this article.)

mation of dense selection layer since the high-concentration polymer will present a barrier to diffusion of the small molecules. And for glass-forming polymers, variable viscosity will lock in the structure at a certain stage of coarsening due to vitrification.

In addition to vitrification, we would also like to extend this methodology to model other solidification mechanisms, such as gelation and crystallization, in the immersion precipitation process. This will require other techniques such as Allen–Cahn equations for non-conserved variables from degree of crystallinity to crystal orientation. This too is an area of ongoing investigation.

It is also hard to rigorously compare model results with experimental work since no model can capture all conditions of the experiments and no experiment can follow exactly the parameters set in the model. For example, the gradient penalty coefficients, which determine the particle size, are very hard to measure. Therefore, at this stage the model can be compared with experiments and predict physical behavior only in a qualitative sense. Development of the model continues toward the goal of a quantitatively accurate predictive tool.

5. Conclusion

The phase field model proposed here is very powerful, with the capability to simulate multiple kinetics phenomena such as diffusion and phase separation by using one set of ternary Cahn–Hilliard equations. The simulation results are very promising in terms of providing a deeper understanding of the immersion precipitation process and theoretical guidance on experiments design membrane formation.

Polymer membrane phase separation during immersion precipitation was simulated in two and three dimensions using this ternary Cahn–Hilliard formulation incorporating a Flory–Huggins homogeneous free energy model. Simulations with different gradient penalty coefficients K_{ij} showed that the dominant wavelength (or interface thickness) is roughly proportional to the square root of $\sum_{i,j} K_{ij}$.

In the water/DMF/PVDF system, the asymmetric structures of simulated membranes in 2D were qualitatively similar to those observed in experiments. Changing the initial composition showed that volume fraction of polymer dominates the morphology and initial composition in the coagulation bath also has impact on the final morphology and kinetics of the immersion precipitation process. Another membrane system, water/acetone/CA, was studied to compare with the water/DMF/PVDF system. The simulated morphology of the CA membrane exhibited larger pore sizes and slower demixing due to weaker interactions.

Simulations with hydrodynamic effects showed that fluid flow destabilizes the top layer in the membrane, with larger surface tension and smaller viscosity making the top layer less stable. 3D simulation results also showed an asymmetric structure, and the pattern of layer breakup in 3D looked similar to experimental surface micrographs.

Acknowledgements

The authors are grateful to Prof. Anne Mayes at MIT for helpful discussions throughout the conduct of this research. The authors acknowledge support for this work given by the Office of Naval Research under contract number N00014-02-1-0343.

References

[1] M. Mulder, Basic Principles of Membrane Technology, Kulwer Academic Publishers, The Netherlands, 1992.
[2] Tompa, Polymer Solutions, Butterworths Scientific Publications, London, 1956.
[3] A.J. McHugh, L. Yilmaz, The diffusion-equations for polymer membrane formation in ternary-systems, J. Appl. Polym. Sci., Polym. Phys. 23 (1985) 1271.
[4] L. Yilmaz, A.J. McHugh, Analysis of nonsolvent solvent polymer phase-diagrams and their relevance tomembrane formation modeling, J. Appl. Polym. Sci., Polym. Phys. 31 (1986) 997.
[5] C. Cohen, G.B. Tanny, S. Prager, Diffusion-controlled formation of porous structures in ternary polymer systems, J. Polym. Sci., Polym. Phys. 17 (1979) 477.
[6] A.J. Reuvers, J.W.A. van den Berg, C.A. Smolders, Formation of membranes by means of immersion precipitation. Part I. A model to describe mass transfer during immersion precipitation, J. Membr. Sci. 34 (1987) 45.
[7] C.S. Tsay, A.J. McHugh, Mass-transfer modeling of asymmetric membrane formation by phase inversion, J. Polym. Sci., Part B: Polym. Phys. 28 (1990) 1327.
[8] L.P. Cheng, D.-J. Lin, C.-H. Shin, A-H. Dwan, C.C. Gryte, PVDF membrane formation by diffusion-induced phase separation-morphology prediction based on phase behavior and mass transfer modeling, J. Polym. Sci., Polym. Phys. 37 (1999) 2079.
[9] Y.D. Kim, J.Y. Kim, H.K. Lee, S.C. Kim, A new modeling of asymmetric membrane formation in rapid mass transfer system, J. Membr. Sci. 190 (2001) 69.
[10] R. Saxena, G.T. Caneba, Study of spinodal decomposition in a ternary polymer–solvent–nonsolvent system, Polym. Eng. Sci. 42 (2002) 1019.
[11] B.F. Barton, A.J. McHugh, Kinetics of thermally induced phase separation in ternary polymer solutions. Part I. Modeling of phase separation dynamics, J. Polym. Sci., Polym. Phys. 37 (1999) 1449.
[12] P.D. Graham, B.F. Barton, A.J. McHugh, Kinetics of thermally induced phase separation in ternary polymer solutions. Part II. Comparison of theory and experiment, J. Polym. Sci., Polym. Phys. 37 (1999) 1461.
[13] B.F. Barton, A.J. McHugh, Modeling the dynamics of membrane structure formation in quenched polymer solutions, J. Membr. Sci. 166 (2000) 119.
[14] A. Akthakul, W.F. MacDonald, A.M. Mayes, Noncircular pores on the surface of asymmetric polymer membranes: evidence of pore formation via spinodal demixing, J. Membr. Sci. 208 (2002) 147.
[15] A. Akthakul, Ph.D. Thesis, MIT, 2003.
[16] J.W. Cahn, J.E. Hilliard, Free Energy of a nonuniform system. Part I. Interfacial free energy, J. Chem. Phys. 28 (1958) 258.
[17] J.W. Cahn, On spinodal decomposition, Acta Metall. 9 (1961) 795.
[18] S.M. Allen, J.W. Cahn, Microscopic theory for antiphase boundary motion and its application to antiphase domain coarsening, Acta Metall. Mater. 27 (1979) 1085.

[19] R. Kobayashi, Modeling and numerical simulations of dendritic crystal-growth, Physica D 63 (1993) 410.
[20] J.A. Warren, W.J. Boettinger, Prediction of dendritic growth and microsegregation patterns in a binary alloy using the phase-field method, Acta Metall. Mater. 43 (1995) 689.
[21] W.L. George, J.A. Warren, A parallel 3D dendritic growth simulator using the phase-field method, J. Comput. Phys. 177 (2002) 264.
[22] J.A. Warren, R. Kobayashi, A.E. Lobkovsky, W.C. Carter, Extending phase field models of solidification to polycrystalline materials, Acta Mater. 51 (2003) 6035.
[23] Y.M. Jin, A. Artemev, A.G. Khachaturyan, Three-dimensional phase field model of low-symmetry martensitic transformation in polycrystal: simulation of zeta'(2) martensite in Aucd alloys, Acta Mater. 49 (2001) 2309.
[24] C.E. Krill III, L.-Q. Chen, Computer simulation of 3-D grain growth using a phase-field model, Acta Mater. 50 (2002) 3057.
[25] M. Honjo, Y. Saito, Numerical simulation of phase separation in Fe–Cr binary and Fe–Cr–Mo ternary alloys with use of the Cahn–Hilliard equation, ISIJ Int. 40 (2000) 914.
[26] D. Jacqmin, Calculation of two-phase Navier Stokes flows using phase-field modeling, J. Comput. Phys. 155 (1999) 96.
[27] S. Balay, W.D. Gropp, L.C. McInnes, B.F. Smith, Efficient management of parallelism in object oriented numerical software libraries, in: E. Arge, A.M. Bruaset, H.P. Langtangen (Eds.), Modern Software Tools in Scientific Computing, Birkhauser Press, 1997.
[28] D.J. Eyre, Systems of Cahn–Hillard equations, SIAM J. Appl. Math. 53 (1993) 1686.
[29] S.M. Allen, J.W. Cahn, Mechanisms of phase transformation within the miscibility gap of Fe-rich Fe Al alloys, Acta Metall. 24 (1975) 426.